Collisional energy transfer in bimolecular ion−molecule dynamics M++(H2; D2; or HD)→(MH++H; MD++D; MH++D; or MD++H)

5 AUTHORS, INCLUDING:

Maciej Gutowski
Heriot-Watt University

201 PUBLICATIONS **6,568** CITATIONS

SEE PROFILE

Mark Roberson
University of Utah

5 PUBLICATIONS **73** CITATIONS

SEE PROFILE

Jon Rusho
University of Utah

8 PUBLICATIONS **32** CITATIONS

SEE PROFILE

Jeffrey Allen Nichols
Oak Ridge National Laboratory

73 PUBLICATIONS **2,391** CITATIONS

SEE PROFILE

Collisional energy transfer in bimolecular ion–molecule dynamics $M^+ + (H_2; D_2;$ or $HD) \rightarrow (MH^+ + H; MD^+ + D; MH^+ + D;$ or $MD^+ + H)$

Maciej Gutowski, Mark Roberson, Jon Rusho, Jeff Nichols,[a] and Jack Simons
Chemistry Department, University of Utah, Salt Lake City, Utah 84112

Guided ion beam kinetic energy thresholds in the ion–molecule reactions $M^+ + H_2 \rightarrow MH^+ + H$, where $M^+ = B^+$, Al^+, and Ga^+ exceed by 0.4–~5 eV the thermodynamic energy requirements or theoretically computed barrier heights of these reactions. In addition, the formation of MD^+ occurs at a significantly lower threshold than MH^+ when M^+ reacts with HD. Moreover, the measured reaction cross sections for production of MH^+ product ions are very small (10^{-17}–10^{-20} cm^2). These facts suggest that a "dynamical bottleneck" may be operative in these reactions. In this work, the eigenvalues of the mass-weighted Hessian matrix, which provide local normal-mode frequencies, are used to identify locations on the ground-state MH_2^+ potential energy surfaces where collisional-to-internal energy transfer can readily take place. In particular, the potential energies at geometries where eigenvalues corresponding to interfragment and to internal motions undergo avoided crossings are related to the kinetic energies of apparent reaction thresholds. This near-resonance energy transfer model, applied to $M^+ + HD$ reactions, displays the experimentally observed preference to form MD^+ at lower collision energies than MH^+ as well as the fact that reaction thresholds may greatly exceed thermodynamic energy requirements. This model explains the small reaction cross sections in terms of high energy content and subsequent dissociation of nascent MH^+ (or MD^+) ions. Although the mass-weighted Hessian matrix is used as a tool in this analysis, the model put forth here is *not* equivalent to a reaction-path Hamiltonian dynamics approach.

I. INTRODUCTION

Guided ion beam measurements[1] of cross sections for reactions of closed-shell ^1S B^+, Al^+, and Ga^+ ions with closed-shell $^1\Sigma_g^+$ H_2, D_2, and $^1\Sigma^+ HD$ have shown features that require interpretation.

(i) The apparent thresholds (i.e., the collision energies where product MH^+ or MD^+ ions are first formed) exceed the minimum thermodynamic energy requirements by significant amounts (e.g., by up to 5 eV for Ga^+).

(ii) In experiments with HD, MD^+ formation displays a lower energy threshold than MH^+.

(iii) The cross sections are small (10^{-17}–10^{-20} cm^2) and are smallest for Ga^+ and largest for B^+.

In the present work, we report findings that relate to these experiments and which allow an interpretation of much of the data in terms of features of the $M^+ + H_2$ potential energy surfaces in regions of strong mode coupling.

In particular, a mass-weighted Hessian analysis of the *local* natural frequencies for *intrafragment* and *interfragment* motions in regions of strong repulsive interactions shows that energy transfer may be the rate limiting step in these reactions. The collision energies needed to access geometries where such dynamical resonances occur are correlated with observed reaction thresholds. Moreover, for $M^+ + HD$ collisions, energy transfer that results in MD^+ formation is shown to occur at lower energy than that

producing MH^+ which involves a higher-energy resonance.

In all cases, the electronic energies in such regions of strong coupling approach (for B^+) or even exceed (for Al^+ and Ga^+) the dissociation energy of H_2. As a result, collisions that access such regions produce MH^+ or MD^+ with a large amount of internal vibrational energy. In fact, these product ions are likely to possess enough internal energy to fragment, thereby reducing the MH^+ (MD^+) yield and the measured reaction cross section (least so for B^+ and most so for Ga^+).

The present use of eigenmodes of the mass-weighted Hessian matrix differs from that embodied in the so-called reaction path Hamiltonian[2] approach. In our model, the critical geometries *need not lie on or even in close proximity to a reaction path*, and have energies far in excess of such a path or of corresponding first-order saddle points (i.e., transition states). Our critical geometries relate more closely to those that are realized in the experiments' very nonequilibrium high-energy ion–molecule bimolecular collisions in which the reagents possess little internal energy.

In Sec. II, we describe the computational methods used to compute the potential energy surfaces, gradient vectors, and mass-weighted Hessian matrices use in this work. In Sec. III, we present and discuss our potential energy surfaces and the reaction energetics they imply, and in Sec. IV, we introduce a dynamical model to simulate the early stages of the $M^+ + H_2$ (D_2 or HD) collisions. Section V describes our primary findings and their relation to the experimental data, and in Sec. VI, we summarize.

---

[a] Also with IBM/FSC Corp. and the Utah Supercomputing Institute.

II. COMPUTATIONAL METHODS

A. Basis sets

For the $B^+ + H_2$ and $Al^+ + H_2$ calculations, the H atom basis was Dunning's augmented correlation consistent (cc) polarized valence triple-zeta (p-VTZ) $(5s2p1d|3s2p1d)$ set of functions.[3] For the B^+ ion, the Dunning $(10s5p2d|4s3p2d)$ augmented cc p-VTZ basis set[3] was used, and a total of 55 contracted Gaussian-type basis functions resulted for BH_2^+. For the Al^+ ion, the McLean–Chandler $(12s9p|6s5p)$ basis set[4] augmented with one $3d$ polarization function (exponent 0.4) was used, and total of 57 contracted Gaussian-type basis functions resulted for AlH_2^+. In the case of Ga^+, the so-called Stevens–Basch–Krauss (SBK) psuedopotential,[5] which treats $1s$, $2s$, and $2p$ orbitals implicitly and $3s$, $3p$, $3d$, $4s$, and $4p$ orbitals explicitly, was used with a $(8L,6d|4L,3d)$ basis. For GaH_2^+, a 6-311G** basis[6] was employed for each H atom, thus giving a total of 46 explicit atomic orbitals.

B. Electronic configurations and wave functions

In generating the potential energy *surfaces*, optimal *geometries*, and local harmonic vibrational *frequencies* reported here, the complete active space (CAS)-based multiconfigurational self-consistent field (MCSCF) method was used to treat correlations among the valence electrons of the MHH^+ system. The six valence orbitals are all those derived from the metal ns, np, and the two H $1s$ orbitals. The *final* electronic *energies* at critical (i.e., optimal) geometries were evaluated at the quadratic configuration interaction including single, double, and approximate triple excitations [QCISD(T)] level to obtain more quantitative estimates of thermodynamic data. In a few situations, convergence difficulties arose in implementing the QCISD(T) calculations, so we resorted to fourth order Møller–Plesset perturbation theory (MP4) for computing our most accurate energies.

As discussed in our earlier work on BH_2^+, no single electronic configuration can describe even the ground state of these systems throughout C_{2v}, $C_{\infty v}$, or C_s reaction paths. For this reason, multiconfigurational methods were required. In the MCSCF calculations, the four valence electrons were distributed, in all ways consistent with overall spatial and spin symmetry, among the six valence orbitals. This process generated 41 electronic configurations of $^1A_1$ symmetry in the C_{2v} point group and 65 electronic configurations of $^1A'$ symmetry in the C_s point group; it yielded 41 configurations in the $C_{\infty v}$ group.

The above MCSCF calculations on BH_2^+ and AlH_2^+ were employed, along with our Utah MESSKit[7(a)] analytical energy derivative and potential energy surface "walking" algorithms[7(b)] to find and characterize (via geometry and local harmonic vibrational frequencies) the local minima, transition states, and reaction paths discussed below. For GaH_2^+, we used the GAMESS program suite,[8] which uses finite-difference methods to compute the Hessian matrix from analytical energy gradients. The QCISD(T) and

MP4 energies were computed using the GAUSSIAN 92 program.[9]

III. REACTION ENERGETICS

A. Potential energy surfaces

1. C_{2v} surfaces

In Figs. 1(a)–1(c) are shown contour potential energy surfaces for the CAS-MCSCF ground electronic states (which have singlet spin and totally symmetric spatial symmetry) of the three $M^+ + H_2$ reactions considered here within C_{2v} symmetry. The axes in the graphs are R the distance in Ångstroms from the M nucleus to the midpoint of the H–H moiety, and r the distance between the two H nuclei (see Fig. 2). The similarities among the three surfaces are striking, with the primary differences being results of (i) B^+ being smaller than Al^+ and Ga^+; and (ii) the H–B–H bonds being stronger than the H–Al–H bonds which are a bit stronger than the H–Ga–H bonds.

In each of these surfaces, four regions are noteworthy:

(i) the asymptotic region ($R > 3$ Å and r near 0.7 Å), where a narrow entrance channel governs the approach of M^+ to H_2 and where the energy variation along the r coordinate is essentially that of an isolated H–H bond, while that along R is rather weakly increasing as R decreases;

(ii) the H–M–H$^+$ linear-ion region near $R=0$ pertaining to the locally stable $^1\Sigma_g^+$ ion (for HAl^+H and HGa^+H, this ion is metastable with respect to $H_2 + Al^+$ or $H_2 + Ga^+$; for HBH^+, the ion lies below $H_2 + B^+$);

(iii) the "barrier" connecting the entrance channel and the linear-ion minimum (the barrier regions are marked by $\times$ in Figs. 1; we refer to them as barriers rather than transition states because, as discussed later, they are second-order saddle points on these surfaces);

(iv) the region of strong interaction where both R and r are relatively small as a result of which the couplings among the internal modes are strong (see the regions marked by Y in Figs. 1).

2. Collinear approach surface

In Fig. 3 is shown a potential energy contour surface (as a function of the distance r_{MH} between the metal and the closest H atom and r) for the collinear approach of B^+ to H–H; the collinear surfaces for Al^+ and Ga^+ display similar features. We found that as r_{MH} decreases from its asymptotic value, the bending vibrational frequency at such collinear geometries is imaginary and its magnitude increases as r_{MH} decreases. Of course, as the angle between the H–H axis and the vector connecting M to the center of the H–H moiety changes from 0° to 90° (i.e., from collinear to C_{2v} geometry), the frequency corresponding to this motion becomes real, reflecting the stability of the C_{2v} regions of the surfaces. The negative curvature along the bending coordinate is caused by the presence of low-lying $2p_\pi$ orbitals on B^+ which, upon bending away from collinear geometry, mix with and lower the energies of occupied valence orbitals thereby lowering the total energy.
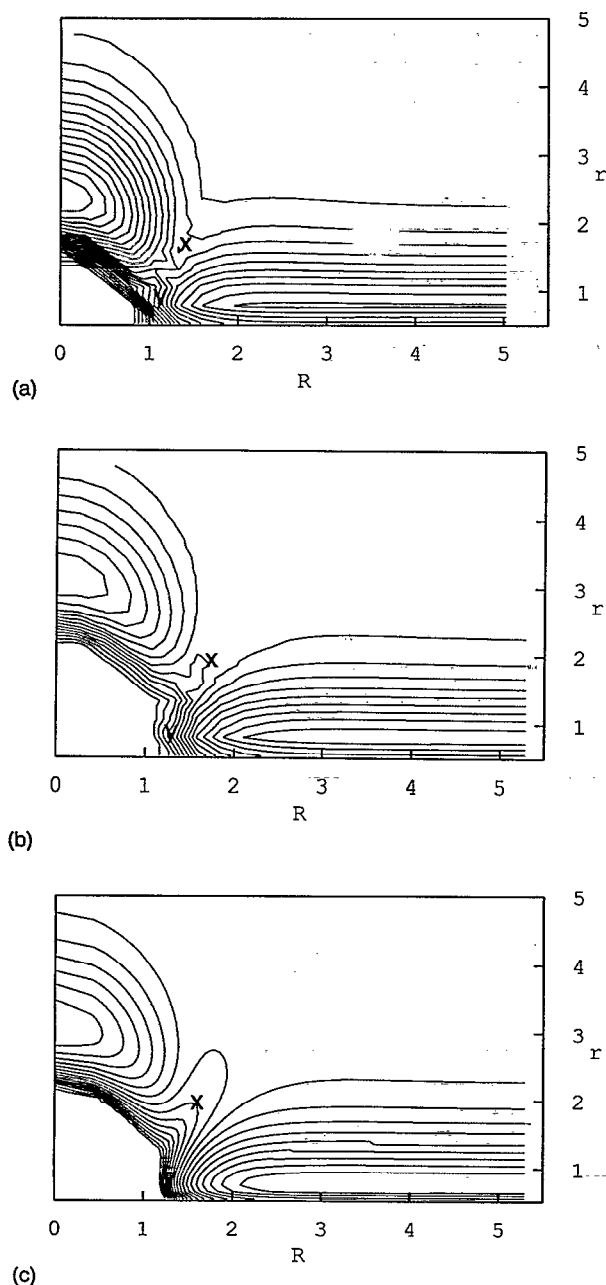
(a)

(b)

(c)

FIG. 1. (a) C_{2v} symmetry contour plot of the ($^1A_1$) ground state energy of $B^+ + H_2$. The R (the distance of B^+ to the center of H–H) and r (H–H distance) axes are in Ångstroms, and the contours are spaced by 10.0 kcal/mol. (b) C_{2v} symmetry contour plot of the ($^1A_1$) ground state energy of $Al^+ + H_2$. The R (the distance of Al^+ to the center of H–H) and r (H–H distance) axes are in Ångstroms, and the contours are spaced by 10.6 kcal/mol. (c) C_{2v} symmetry contour plot of the ($^1A_1$) ground state energy of $Ga^+ + H_2$. The R (distance of Ga^+ to the center of H–H) and r (H–H distance) axes are in Ångstroms, and the contours are spaced by 10.4 kcal/mol. In (a)–(c), the symbol X is used to denote the location of the barrier, and Y is used to denote the region of strong mode mixing (see the text).

The fact that the potential surface becomes more and more unstable to rotating the H–H bond axis away from the M^+ ion as r_{MH} decreases means that flux incident toward such collinear approaches will be moved, by forces directed away from linear geometries, toward the "insertive" C_{2v} type geometries. For this reason, it is unlikely
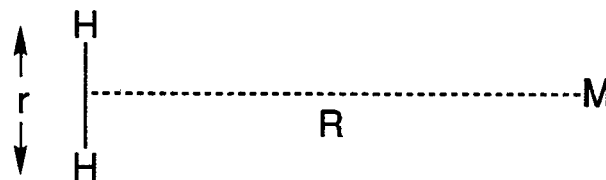

FIG. 2. The coordinate system used to label C_{2v} geometries.

that linear or near-linear orientations play important roles in the $M^+ + H_2 \rightarrow MH^+ + H$ reactions *even though* there is no barrier along such paths in excess of the thermodynamic energy difference (calculated here to be 61, 91, and 94 kcal/mol for B^+, Al^+, and Ga^+, respectively). It is for this reason that we focus the majority of our study and analysis on the C_{2v} (and near) pathways, although these paths do experience barriers in excess of thermodynamic requirements.

B. Reaction thermochemistry

In Tables I(A)–I(C) are displayed our QCISD(T) calculated (and, where known, the experimental) values for the relative energies of the reactant $M^+ (ns^2;^1S) + H_2$, excited-state reactant $M^+ (nsnp;^{3,1}P) + H_2$, and product $MH^+ + H$ and HMH^+ species. In all cases, the energies are derived from electronic energies; no zero-point corrections are included.

The lowest excited ^3P and ^1P states of M^+ are listed because they give rise to excited $^{3,1}B_2$, $^{3,1}A_1$, and $^{3,1}B_1$ states of C_{2v} MH_2^+ which, in turn, affect the ground-state reaction dynamics via second-order Jahn–Teller coupling[10] to or intersections with the ground $^1A_1$ state as described later in this paper. It is essential that our calculations place these excited states reasonably accurately if our inferences about the ground-state dynamics are to be reliable.

An important point to note about these data is that the *experimental thresholds* for producing $MH(D)^+ + H(D)$ *do not correlate* with the thermodynamic energy differences
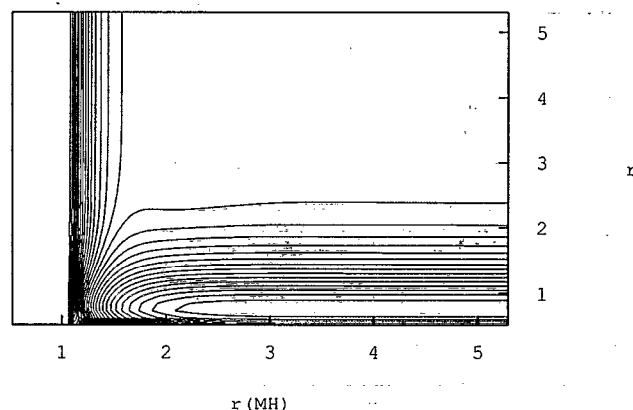

FIG. 3. Contour plot of the ($^1A_1$) ground state energy of $B^+ + H_2$ for collinear geometries. The r(MH) (distance of B^+ to the nearest H atom) and r (H–H distance) axes are in Ångstroms, and the contours are spaced by 6.3 kcal/mol.

TABLE I. Electronic states energies (kcal/mol) measured with respect to (A) B$^+$(^1S)+H$_2$($^1\Sigma_g^+$); (B) Al$^+$(^1S)+H$_2$($^1\Sigma_g^+$); and (C) Ga$^+$(^1S)+H$_2$($^1\Sigma_g^+$).

(A)	Species[a]	This work[b]	Experiment[a]
	B$^+$(^1S)+H$_2$($^1\Sigma_g^+$)	0.0	0.0
	B$^+$(^1S)+2H(^2S)	109	110
	B$^+$(^3P)+H$_2$($^1\Sigma_g^+$)	107	107
	B$^+$(^1P)+H$_2$($^1\Sigma_g^+$)	215	210
	BH$^+$($^2\Sigma$)+H	ΔE_{thermo}=61	61
	HBH$^+$($^1\Sigma_g^+$)	−60	
	B$^+\cdots$H$_2$ barrier	73	
(B)	Species[a]	This work[b]	Experiment[a]
	Al$^+$(^1S)+H$_2$($^1\Sigma_g^+$)	0.0	0.0
	Al$^+$(^1S)+2H(^2S)	109	110
	Al$^+$(^3P)+H$_2$($^1\Sigma_g^+$)	105	107
	Al$^+$(^1P)+H$_2$($^1\Sigma_g^+$)	180	171
	AlH$^+$($^2\Sigma$)+H	ΔE_{thermo}=91	
	HAlH$^+$($^1\Sigma_g^+$)	12	
	Al$^+\cdots$H$_2$ barrier	104	
(C)	Species[a]	This work[b]	Experiment[a]
	Ga$^+$(^1S)+H$_2$($^1\Sigma_g^+$)	0.0	0.0
	Ga$^+$(^1S)+2H(^2S)	109	110
	Ga$^+$(^3P)+H$_2$($^1\Sigma_g^+$)	123	137
	Ga$^+$(^1P)+H$_2$($^1\Sigma_g^+$)	196	202
	GaH$^+$($^2\Sigma$)+H	ΔE_{thermo}=94	
	HGaH$^+$($^1\Sigma_g^+$)	20	
	Ga$^+\cdots$H$_2$ barrier	105	

[a]C. E. Moore, *Tables of Atomic Energy Levels* (Natl. Stand. Ref. Data Serial, Natl. Bur. Stand., 35/V.I, 1971); K. P. Huber, G. Herzberg, *Molecular Spectra and Molecular Structure, IV, Constants of Diatomic Molecules* (Van Nostrand–Reinhold, New York, 1979).

[b]Based on QCISD(T) data except for the ^1P state where projected fourth-order Møller–Plesset (PMP4) perturbation theory was used due to difficulties in the QCISD(T) convergence.

$$\Delta E_{\text{thermo}}=E[\text{MH(D)}^+]+E[\text{H(D)}]-E(\text{M}^+)$$
$$-E[\text{H}_2(\text{D}_2 \text{ or HD})]$$

which appear in the fifth rows of Table I. *Nor do these thresholds agree* with the locations of the "barriers" on the potential energy surfaces shown in Fig. 1 and listed in the seventh rows of Table I. These facts make it clear that a "dynamical" rather than energetic constraint must be operative in determining the experimental thresholds which exceed by from ~0.4 eV (for BD$^+$ formation) to as much as 5 eV (for GaD$^+$ formation), the thermodynamic energy requirements. It is for this reason that we must now turn our attention to the *dynamics* of the M$^+$+H–H collision.

IV. DYNAMICS

A. Experimental conditions and their implications

1. Initial conditions

The guided ion beam experiments of Armentrout and co-workers[1] involve collisions in which the H$_2$ (D$_2$ or HD) and M$^+$ reagents' *internal* (vibrational, rotational, and electronic) degrees of freedom usually exist in or close to thermal equilibrium near room temperature. Therefore, nuclear motions along these degrees of freedom are re-

stricted, in the early stages of the ion–molecule collision, to narrow ranges approximately characterized by the corresponding classical turning points. As a result, the most important areas of the potential energy surface in the entrance channel region are those for which such internal modes do not deviate greatly from their most probable values.

In contrast, the relative kinetic energy between the M$^+$ ion and its H$_2$ (or D$_2$ or HD) collision partner is very large in comparison with thermal energies. This collision energy, and its associated momentum, has components along three directions: (i) the M-to-H (or D) axis (r_{MH}); (ii) the other M-to-H (or D) axis ($r_{\text{MH}'}$); and (iii) the out-of-molecular plane angular coordinate ϕ. Explicitly, the classical collisional kinetic energy in an M$^+$+A–B encounter is

$$T_{\text{collision}}=\frac{1}{2}\frac{m_M(m_A+m_B)}{m_A+m_B+m_M}\left(\frac{dY}{dt}\right)^2=T_{\text{lab}}\frac{(m_A+m_B)}{m_A+m_B+m_M},$$

where the kinetic energy of the M$^+$ ion as measured (and experimentally controlled) in a lab-fixed coordinate system is

$$T_{\text{lab}}=\frac{m_M}{2}\left(\frac{dY}{dt}\right)^2.$$

Here, m_M, m_A, and m_B represent the masses of the three particles, and Y the separation of M$^+$ to the center of mass of the A–B pair. The collisional kinetic energy can be decomposed into components describing motion of M$^+$ along the r_{MA} and r_{MB} axes as follows:

$$T_{\text{MA}}=T_{\text{lab}}\frac{m_A}{m_A+m_M}\cong T_{\text{collision}}\frac{m_A}{m_A+m_B}\cong\frac{m_A}{2}\left(\frac{dr_{\text{MA}}}{dt}\right)^2,$$

$$T_{\text{MB}}=T_{\text{lab}}\frac{m_B}{m_B+m_M}\cong T_{\text{collision}}\frac{m_B}{m_A+m_B}\cong\frac{m_B}{2}\left(\frac{dr_{\text{MB}}}{dt}\right)^2,$$

where the second equalities are only approximate because they assume $m_M\gg m_A+m_B$.

2. Role of kinetic energy along collision degrees of freedom

The above decomposition of the collision energy has been used[1] to rationalize the occurrence of different energy thresholds for production of MH$^+$ and MD$^+$ in M$^+$+HD reactions, the idea being that there is more energy along the r_{MD} axis (2/3 $T_{\text{collision}}$) than along the r_{MH} axis (1/3 $T_{\text{collision}}$), so MD$^+$ can be formed at lower total collision energies. However, this model predicts that the difference in thresholds for MH$^+$ and MD$^+$ should differ by a factor of 2 (with the MD$^+$ threshold occurring at one-half the collision energy of MH$^+$), and that for M$^+$+H$_2$ or M$^+$+D$_2$, where there are 1/2 $T_{\text{collision}}$ and 2/4 $T_{\text{collision}}$ along the r_{MH} and r_{MD} axes, the thresholds should be even different than in the HD case. These quantitative details are not observed[1] in the experimental data, although there are significant differences (much more than zero-point energies can account for) in the HD, H$_2$, and D$_2$ thresholds.

The primary difficulty with using this fractional collision energy T_{MB} concept is that it ignores how the potential energy V depends on the two independent r_{MH} and r_{MD} axes. If V were a strong function of one of these coordinates (e.g., of the distance from M^+ to the nearest H or D center), and depended weakly, if at all, on the other distance, then this decomposition of $T_{collision}$ would make more sense. When the kinetic energy along the "important" M-to-H (or D) coordinate was adequate to overcome any barrier in V along this same coordinate, reaction could take place. However, for the reactions at hand, V depends on the two r_{MH} and $r_{MH'}$ (or r_{MD}) distances in a symmetrical fashion; i.e., the electronic energy remains the same if r_{MH} and $r_{MH'}$ are interchanged. Moreover, V is a strong function of both distances, at least within the entrance channel where the collision-to-internal energy transfer is initiated. As a result, kinetic energy along both r_{MH} and $r_{MH'}$ is required to access regions of the potential where reaction can occur; neither T_{MH} nor $T_{MH'}$ alone is adequate. It is for these reasons that consideration of the kinetic energy alone does not adequately explain the isotope effects on thresholds.

Nevertheless, the different masses of the H and D isotopes do, in fact, have important effects on the thresholds for MD^+ and MH^+ formation, but not because of the reasons outlined above. The hydrogenic masses m_A and m_B, as well as the H–D, H_2, or D_2 reduced mass μ, appear in the kinetic energy, approximately (see Sec. IV G for more detail) as

$$T \cong \frac{m_A}{2} \left(\frac{dr_{MA}}{dt}\right)^2 + \frac{m_A}{2} \left(\frac{dr_{MB}}{dt}\right)^2 + \frac{\mu}{2} \left(\frac{dr}{dt}\right)^2.$$

As discussed later in this paper, so-called mass-weighted coordinates $r' = \sqrt{\mu}\, r$, $r'_{MD} = \sqrt{m_D}\, r_{MD}$, and $r'_{MH} = \sqrt{m_H}\, r_{MH}$ can be introduced after which the *total* energy $H = T + V$ is expressed as

$$H = \frac{1}{2} \left(\frac{dr'_{MA}}{dt}\right)^2 + \frac{1}{2} \left(\frac{dr'_{MB}}{dt}\right)^2 + \frac{1}{2} \left(\frac{dr'}{dt}\right)^2 + V(r'_{MA}, r'_{MB}, r').$$

In this form, isotopic differences disappear from T and appear only in the different dependence of V on r'_{MA}, r'_{MB}, and r'. Although V depends on r_{MA} and r_{MB} in a symmetrical manner, its dependence on r'_{MA} and r'_{MB} may be asymmetric and reflects the A and B masses. It is these mass dependencies that produce isotope effects in the local normal-mode frequencies derived from such a Hamiltonian, and it is these mass effects that we think more correctly explains the isotope effects on reaction thresholds.

B. Entrance-channel reaction dynamics

The potential energy function along the *relative-motion* degrees of freedom is slowly varying as the collision begins (i.e., at large R and small r). As the collision progresses, these three degrees of freedom evolve in a manner that produces significant forces (i.e., changes in potential) along r_{MH} and $r_{MH'}$. Keeping in mind that essentially all of the initial momentum is directed along these "soft modes,"

and recalling that restoring forces strive to preserve C_{2v} symmetry, we direct attention to flux moving with high initial energy and velocity along both r_{MH} and $r_{MH'}$ and little energy along the r axis (because of the low vibrational energy of the H_2 reagents).

C. Entering the region of strong interaction

As flux progresses up the entrance channel to higher potential energy, the radial kinetic energy and momenta along r_{MH} and $r_{MH'}$ decrease, but lack of coupling between the R and r directions [i.e., $(\partial^2 E/\partial R \partial r) \approx 0$ as illustrated clearly in Fig. 1] makes energy (and momentum) transfer from the relative-motion modes to the transverse r-dominated mode very ineffective.

However, as flux moves to even smaller R values, a region of space is reached where energy transfer can occur. This region is characterized *not* only by existence of off-diagonal $\partial^2 E/\partial R \partial r$ coupling on the potential energy surfaces as shown in Fig. 1, but also by near degeneracies in the eigenvalues of the mass-weighted Hessian (MWH) matrix (see below) evaluated at such geometries.

These statements now need to be justified by introducing and using the MWH matrix as a device for analyzing the dynamical resonances that permit energy transfer and subsequent chemical reaction to occur.

D. The Hessian as a local approximation to the potential energy

The Hessian matrix, evaluated at a geometry in the region of strong interaction (denoted $\{x_k^0\}$) and expressed in terms of the $3N$ Cartesian coordinates $\{x_k\}$ of the N atoms is

$$H'_{k,m} = (\partial^2 E/\partial x_k \partial x_m)_{x_k^0}.$$

The gradient vector

$$F'_k = (\partial E/\partial x_k)_{x_k^0}$$

evaluated at this same point gives the slope of the energy along the Cartesian directions x_k. Of course, the values of this matrix and vector depend strongly on where these derivatives are evaluated; at a point $\{x_k^0\}$ in the strong interaction region, $\{F'_k\}$ has large components along the interfragment coordinates.

These constructs allow the potential energy surface $V(x_k)$ to be approximated to the point $\{x_k^0\}$ as a Taylor series

$$V(x_k) = V(\{x_k^0\}) + \sum_k F'_k \delta x_k + 1/2 \Sigma_{k,m} H'_{k,m} \delta x_k \delta x_m,$$

where δx_k means the deviation of x_k from the value x_k^0.

E. The kinetic energy in mass-weighted coordinates

Of course, the kinetic energy T can also be written in terms of the $3N$ Cartesian displacement coordinates $\{\delta x_k\}$. However, if so-called *mass-weighted coordinates*

$$y_k = \sqrt{m_k} x_k$$

are introduced, where m_k is the mass of the nucleus to which the coordinate x_k pertains, the kinetic energy can be written as a sum

$$T = \sum_k \frac{1}{2} m_k \left(\frac{dx_k}{dt}\right)^2 = \sum_k \frac{1}{2}\left(\frac{dy_k}{dt}\right)^2$$

of $3N$ terms each of which has the same (unit) mass factor. In this form, the matrix representation of T within the $\{y_k\}$ coordinate basis is $1/2$ times the unit matrix; $T_{k,m} = 1/2\delta_{k,m}$. By so treating the kinetic energy in a manner that assigns equal mass to all $3N$ degrees of freedom, the potential energy function alone governs the natural frequencies of motion of the system.

F. The mass-weighted Hessian

In terms of these $\{y_k\}$ coordinates, the local quadratic approximation to the potential energy is given by

$$V(y_k) = \sum_k F_k \delta y_k + 1/2 \sum_{k,m} H_{k,m}\delta y_k \delta y_m,$$

where F_k is the gradient

$$F_k = (\partial E/\partial y_k)_{x_k^0} = (m_k)^{-1/2}(\partial E/\partial x_k)_{x_k^0}$$

of the electronic energy along the y_k coordinate, $H_{k,m}$ is the matrix of second derivatives with respect to the y_k variables

$$H_{k,m} = (\partial^2 E/\partial y_k \partial y_m)_{x_k^0} = H'_{k,m}(m_k m_m)^{-1/2},$$

and δy_k is the displacement along the y_k coordinate from the point at which the derivative is evaluated. The matrix $\{H_{k,m}\}$ is called the *mass-weighted Hessian* matrix (MWH), and $\{F_k\}$ is the gradient vector in mass-weighted coordinates. Notice that $H_{k,m}$ has units of s^{-2} because δy_k has units of $gm^{1/2}$ cm; therefore, the eigenvalues of $\{H_{k,m}\}$ introduced in the next section have units of s^{-2}, or frequency squared.

G. The classical equations of motion

A classical Hamiltonian

$$H = T + V$$

$$= \sum_k \frac{1}{2}\left(\frac{d\delta y_k}{dt}\right)^2 + \sum_k F_k \delta y_k + 1/2 \sum_{k,m} H_{k,m}\delta y_k \delta y_m$$

treatment can be used to describe the (local) motion of the $3N$ degrees of freedom. The Newton equations of motion then read

$$\frac{d^2\delta y_k}{dt^2} = -F_k - \sum_m H_{k,m}\delta y_m.$$

The linear-plus-quadratic form of the potential is a reasonable representation of the potential along *internal* degrees of freedom that undergo small-amplitude motions about their equilibrium positions. However, this is an unreasonable *global* representation for the potential along interfragment degrees of freedom. The latter coordinates are not bounded by the potential at large R, whereas the quadratic terms above, if $\{H_{k,m}\}$ is positive definite, would

constrain the interfragment coordinates at large separations. The model potential produces harmonic oscillatory motion even along the interfragment degrees of freedom, although they really undergo collisions with a single close encounter between the fragments. Nevertheless, as shown below, the description of interfragment degrees of freedom (i.e., r_{MH} and $r_{MH'}$) provided by these equations of motion is useful in analyzing the dynamics *local* to the points $\{x_k^0\}$ of strong interaction and for the short duration of the collision.

1. The MWH eigenmode basis

a. Eigenmodes of the full MWH. To make further progress, we now introduce, for reasons that will soon become clear, the (unitary) matrix $u_{k,j}$ that diagonalizes the full $3N \times 3N$ dimensional MWH matrix $\{H_{k,m}\}$

$$\sum_m H_{k,m} u_{m,j} = \omega_j^2 u_{k,j},$$

and we denote the *nonzero* eigenvalues by ω_j^2 ($j = 1,2,...,3N$-5 or $3N$-6). The MWH matrix will also have five or six eigenvalues and corresponding eigenvectors belonging to the translation and rotation of the entire MHH^+ species. Using well-known techniques,[2] these five or six modes (whose components we denote $t_{m,k}$; $k = 1$, $2,...5$, or 6) can be removed explicitly from consideration by projecting them from the MWH matrix.

b. Relation to bases used in reaction path Hamiltonian approaches. In the reaction path Hamiltonian[2] treatment of dynamics and in so-called gradient extremal[11] methods, one defines a "path," usually embodied in a series of finite "steps" connecting a transition state to reactant and product local minima. For the species under study, such paths would lie in the narrow entrance channels shown in Fig. 1 and would proceed smoothly up this valley to the "barriers" shown in these figures, subsequently passing down to the H–M–H⁺ linear–molecule minimum geometries. The ideas underlying introducing such a path include the assumptions (i) that dynamical motions transverse to the path may be treated as undergoing bound, approximately harmonic movement, and (ii) that movement along the path cannot be so treated because there is no barrier or restoring force at large interfragment distances. As a result, it is common to approximate the full dynamics in terms of interfragment scattering along the reaction path coupled to approximately harmonic motion transverse to the path.

In generating algorithms to follow such paths, both methods choose the direction u^0 (a unit vector whose $3N$ components are denoted $\{u_k^0\}$) along which the gradient lies to define one "special" direction. Within the $3N$-7 (or $3N$-6) dimensional space that is orthogonal to the gradient and to the five or six translation and rotation vectors $\{t_{m,k}\}$ a set of unit vectors $\{u^p\}$ for $p = 1, 2,..., 3N$-7 or $3N$-6 (each having $3N$ components $\{u_k^p; k = 1,2,...,3N\}$) is then introduced.

In the reaction path approach,[2] the vectors $\{u^p\}$ are *chosen* to diagonalize the MWH within the $3N$-7 or $3N$-6 dimensional space they span

$$\sum_m H_{k,m} u_m^{p'} = \omega_p'^2 u_k^p; \quad p = 1, 2, \ldots 3N\text{-}7 \text{ or } 3N\text{-}6.$$

The component of $H_{k,m}$ lying along the gradient $\Sigma_{k,m} u_k^0 H_{k,m} u_k^0 = H^0$, together with the magnitude F of the gradient is used to approximate the "shape" of the potential V along the $\mathbf{u}^0$ direction (whose displacement is denoted ds), and the transverse local harmonic frequencies $\{\omega_p'\}$ are used to approximate V along the $\{\mathbf{u}^p\}$ directions (whose displacements are denoted $\{Q^p\}$),

$$V \cong F \, ds + 1/2 \, ds^2 H^0 + 1/2 \sum_p \omega_p'^2 |Q^p|^2.$$

As one then steps along this reaction path, one evaluates the gradient and MWH at each successive geometry and uses the "current" values to define the terms in the above approximation to V. For this reason, H^0, $\{\omega_p'\}$, F, and $\{Q^p\}$ all depend on the current position (s) along the reaction path coordinate and thus evolve as one moves along the path.

In contrast, when employing the gradient extremal method[11] to define a reaction path, one first seeks that geometry, along a constant energy contour [which one imposes via the Lagrange multiplier condition 2λ (V −const.)], at which the magnitude of the gradient is an extremum. This condition is expressed by setting to zero the derivatives of

$$|\nabla V|^2 - 2\lambda(V - \text{const.})$$

with respect to each of the $3N$ y_k coordinates. Doing so produces

$$\sum_m \frac{\partial^2 V}{\partial y_k \partial y_m} \frac{\partial V}{\partial y_m} = \lambda \frac{\partial V}{\partial y_k},$$

which shows that at the point along the contour where the gradient's length is extremized, the gradient vector itself must be an eigenvalue of the MWH. In fact, the minimum of the gradient norm occurs when the gradient lies along the lowest (nonzero) eigenmode of the MWH; this is the direction most often used[11] in defining the gradient extremal reaction path.

The two reaction paths outlined above differ even though they both focus on the gradient direction. In the latter,[11] the gradient direction $\mathbf{u}^0$ is itself an eigenmode direction of the full MWH. As a result, the elements of the MWH connecting $\mathbf{u}^0$ to the remaining $3n - 7$ or $3N - 6$ "internal" mode directions $\{\mathbf{u}^p\}$ vanish explicitly

$$\sum_{k,m} u_k^0 H_{k,m} u_m^{p'} = 0.$$

If $\{\mathbf{u}^p\}$ are *chosen* as eigenvalues of the MWH within the space they span

$$\sum_m H_{k,m} u_m^{p'} = \omega_p'^2 u_k^p,$$

then each of the vectors $\mathbf{u}^0$ and $\{\mathbf{u}^p\}$ are eigenvectors of the *full* MWH having nonzero eigenvalues because the coupling terms $\Sigma_{k,m} u_k^0 H_{k,m} u_m^{p'}$ vanish. In the reaction path

Hamiltonian approach, these off-diagonal coupling elements do not vanish, but are ignored in building the local approximation to the potential V.

In our approach to the energy transfer bottleneck problem, neither the reaction path Hamiltonian's path nor the gradient extremal path are appropriate to introduce. The large radial kinetic energies produced in the guided ion beam experiments cause M+ + HH trajectories to access geometries far from either path. In particular, such trajectories evolve to much smaller R values and have r values constrained closer to the equilibrium bond length of H₂ than characterize either reaction path. Therefore, the gradient at any point accessed by such high kinetic energy trajectories *cannot* be expected to lie along or even near the direction that characterizes a reaction path. An examination of the gradients along the paths used in our study (chosen to represent high energy collisions) show they can have substantial components along both (i) the interfragment coordinates and (ii) the intrafragment modes that might be approximated well in a local harmonic manner. For this reason, we believe it is *inappropriate*, in our case, to introduce any decomposition of the inter- and intrafragment dynamics that uses the gradient to define a "special" direction that is treated differently than others. Hence, in the development pursued below, we do not decompose the $3N$-6 or $3N$-5 dimensions of the MWH into one special direction and $3N$-7 or $3N$-6 in others; we work with the full MWH matrix.

c. Classical Newton equations of motion. Returning now to the issue of expressing the dynamics of motion on an approximate potential energy surface given in terms of the local gradient and MWH, the $\{y_k\}$ basis Newton equations are multiplied by $u_{k,j}$ and summed over k to obtain equations of motion

$$\frac{d^2 \delta A_j}{dt^2} = -f_j - \omega_j^2 \delta A_j$$

for the components δA_j of δy_k along the normalized eigenmodes of the MWH

$$\delta A_j = \sum_k u_{k,j} \delta y_k.$$

Here, f_j is the projection of the $\{F_k\}$ force vector along the jth eigenmode of the MWH

$$f_j = \sum_k u_{k,j} F_k.$$

2. The MWH model dynamical system for bimolecular dynamics

The equations derived above

$$\frac{d^2 \delta A_j}{dt^2} = -f_j - \omega_j^2 \delta A_j$$

specify the time evolution of a *model* dynamical system containing $3N$-5 or $3N$-6 modes that undergo sinusoidal motions (if ω_j^2's are positive)

$$\delta A_j(t) = \delta A_j(\text{eq}) + A_j(t=0)\cos(\omega_j t)$$

at frequencies ω_j (s⁻¹) about equilibrium positions

$$\delta A_j(\text{eq}) = \frac{-f_j}{\omega_j^2}.$$

Here, $\delta A_j(t=0)$ is the amplitude of motion along the jth normal mode, which is, in turn, related to the total energy E_j contained in that mode

$$E_j = \frac{1}{2}\left|\frac{d\delta A_j}{dt}\right|^2 + \frac{1}{2}\,\omega_j^2|\delta A_j - \delta A_j(\text{eq})|^2$$

$$= \frac{1}{2}\,\omega_j^2|A_j(t=0)|^2[\sin^2(\omega_j t) + \cos^2(\omega_j t)],$$

so

$$A_j(t=0) = \sqrt{\frac{2E_j}{\omega_j^2}}.$$

Let us now examine how this model dynamics relates to the M⁺ + A–B collision dynamics under study.

a. Internal modes. In the example at hand, forces along *internal modes* of the ion or its collision partner (i.e., the r-dominant H–H vibration) are *small* in the early stages of the collision because of the small excursions experienced by these degrees of freedom, so oscillatory motion does indeed take place about the equilibrium position. Also, the energy content of these modes is small, so the corresponding amplitudes $A_j(t=0)$ will be small and can be estimated as

$$A_j(t=0) = \sqrt{\frac{2E_{kT}}{\omega_j^2}},$$

where kT is the thermal energy. For these modes, the picture provided by the MWH model is appropriate and easily understood.

b. Relative-motion modes. In contrast, the MWH picture of the *interfragment* motions (i.e., the modes arising from r_{MH} and $r_{MH'}$) requires further examination. At points $\{x_k^0\}$ on the potential energy surface where strong coupling between the r_{MH} or $r_{MH'}$ and internal (r) modes are likely, the forces f_j along interfragment coordinates will be large and repulsive (see Fig. 1). The curvature of the potential surface along these directions, as reflected in the corresponding eigenvalues of the MWH, will be positive (see later) and substantial.

The MWH dynamical model treats these interfragment degrees of freedom as also undergoing harmonic motion, *but* about a minimum that is far removed (by an amount $-f_j/\omega_j^2$) from the point $\{x_k^0\}$ and which lies $f_j^2/2\omega_j^2$ in energy below its value at $\{x_k^0\}$. Clearly, this description of the interfragment motion is not *globally* correct because the true collisional dynamics involves a single encounter between the fragments, not a sinusoidal series of such encounters. Nevertheless, if used only for the brief time interval during which strong mode coupling is realized, this does give a useful *local model* of the true dynamics because

(i) it describes adequately the potential surface (i.e., the forces and *local* natural frequencies of motion) near points $\{x_j^0\}$, where mode coupling is strongest; and

(ii) it includes the correct relative kinetic energies along all modes.

For these reasons, the approximate MWH Newton equations can be used to obtain the time evolution of the system for the (brief) duration of the collision during which the M⁺ ion resides in this repulsive region of the potential surface and during which energy transfer is possible.

H. Avoided crossings of MWH eigenvalues

At geometries where a (local) relative-motion MWH eigenvalue ω_s and an internal-mode eigenvalue ω_{int} undergo an avoided crossing, there is enhanced probability of energy transfer from the collision coordinate to the mode associated with ω_{int}. In such cases, one can think of the dynamics of two coupled oscillators having frequencies ω_s and ω_{int}, whose coordinates obey

$$\frac{d^2\delta A_s}{dt^2} = -f_s - \omega_s^2\delta A_s - \Omega\delta A_{int},$$

$$\frac{d^2\delta A_{int}}{dt^2} = -f_{int} - \omega_{int}^2\delta A_{int} - \Omega\delta A_s,$$

where Ω (with units of s⁻²) denotes the coupling between the two coordinates. In the absence of coupling, these two coordinates would undergo simple sinusoidal motions about their own equilibrium positions and at their own frequencies.

However, as shown in many elementary classical mechanics texts,[12] when coupling is present, the time evolution involves two new characteristic frequencies $\omega_{\pm}$. In the limit where $\omega_s \cong \omega_{int} \equiv \omega_0$ (i.e., when the two natural frequencies would cross if coupling were absent), the two new frequencies are given by

$$\omega_{\pm} = \sqrt{\omega_0^2 \pm \omega},$$

which reduces to

$$\omega_{\pm} = \omega_0 \pm \frac{\Omega}{2\omega_0}$$

if $|\Omega| \ll \omega_0^2$, as it is for the cases considered below.

If energy E is deposited initially into the collision mode s, then the two modes will evolve in time as

$$\delta A_s(t) - \delta A_s(\text{eq}) = \sqrt{\frac{2E}{\omega_0^2}}\cos\left(\frac{\Omega t}{2\omega_0}\right)\cos(\omega_0 t),$$

$$\delta A_{int}(t) - \delta A_{int}(\text{eq}) = \sqrt{\frac{2E}{\omega_0^2}}\sin\left(\frac{\Omega t}{2\omega_0}\right)\sin(\omega_0 t).$$

For short times t, the $\delta A_s(t)$ mode contains much energy and its coordinate oscillates at frequency ω_0. As time evolves, the $\delta A_{int}(t)$ mode gains amplitude, and once

$$\frac{\Omega t}{2\omega_0} = \frac{\pi}{2},$$

this mode has acquired all of the amplitude (and hence energy) that the $\delta A_s(t)$ mode originally had. One thus says that in a time interval $\tau = (\pi\omega_0)/\Omega$ the energy transfer takes place; alternatively, the *rate* of energy transfer is

$$\text{rate} = \frac{\Omega}{\pi\omega_0}.$$

This result would be most relevant *if* the coupling Ω were operative as detailed above throughout the entire sinusoidal motions of the two oscillators. However, to model the situation at hand, it is more proper to allow Ω to act *only for the narrow range* of interfragment distances ΔR, where the two modes undergo their avoided crossing. A modification of the above rate expression that allows Ω to act only for that fraction f of an oscillation [of $\sin(\omega_0 t)$] that the collision resides within ΔR is given as follows:

$$\text{rate} = \frac{\Omega}{\pi\omega_0} f = \frac{\Omega}{\pi\omega_0} \frac{\Delta R}{v} \omega_0 = \frac{\Omega \Delta R}{\pi v}.$$

Here $(\Delta R)/v$ is the residence time of the trajectory with speed v in the range ΔR, and ω_0 is the inverse of the time it takes to make one oscillation. Of course, the speed v can be expressed in terms of the energy E in the s mode, and the potential V at the geometry where the avoided crossing occurs.

A substantial body of experience in the classical dynamics of multimode systems[13] has shown that when the (local) natural frequencies of two degrees of freedom become nearly equal ($\omega_s \cong \omega_{\text{int}} \equiv \omega_0$), energy transfer between these modes is most likely. Within a quantum dynamics treatment, energy transfer is facile when two modes have equal or nearly equal energy *spacings*. The classical and quantum points of view are easily seen to be consistent when, as here, a *local quadratic* treatment (which incorporates the true local forces and curvatures) is used for the potential. In such a case, the resultant *harmonic* frequencies ω_s and ω_{int} give *both* the natural frequencies of the corresponding periodic motions and the frequency *spacings* between neighboring quantum states that differ by a unit quantum number. Thus the resonance condition discussed above can be viewed either as near equality between two natural periodic oscillation times or as near equality between two quantum-state energy spacings.

It is also known that movement through regions of such near degeneracy must have a "contact" or "residence" time $(\Delta R)/v$ long enough to permit the coupling between the two modes that undergo the avoided crossing to effect a transition. If movement through this region is extremely fast, energy transfer is unlikely. In the following section, such avoided crossings are used to explore under what conditions such energy transfer can readily occur.

V. FINDINGS AND RELATION TO EXPERIMENTS

A. Avoided crossings

We show the eigenvalues of the locally calculated MWH for $M^+ = B^+$, Al^+, and Ga^+ in Figs. 4(a)–4(c) and, in each case, results for all three isotopes (H, HD, and DD) are shown. In Fig. 4(d), the eigenvalues of the MWH

are shown for the collinear approach path for comparison. In all cases, the distance r between the two hydrogenic centers was held fixed at the equilibrium value in H_2 0.755 Å. This was done because the geometries that play critical roles in determining where energy transfer occurs are *not* those in which all nuclear coordinates are relaxed, but those that would be realized during high-energy ion–molecule collisions such as those taking place in the guided ion beam experiments. At least in the early stage of such collisions, before energy transfer has taken place, the H–H (or H–D or D–D) distance deviates only slightly from 0.755 Å.

In all of Fig. 4, the relative-motion eigenvalues are very small at large R, where the forces between M^+ and H_2 (or D_2 or HD) are quite weak, and the internal-mode eigenvalue is large. As R decreases, the former eigenvalues increase because the interfragment forces increase, and eventually one or more avoided crossings (or actual crossing for the H_2 and D_2 cases in which the asymmetric stretching mode is uncoupled by symmetry from the two a_1 modes) take place.

The energy transfer ideas reviewed above imply that facile energy (and momentum) transfer from the (soft) r_{MH} and $r_{\text{MH}'}$ collision eigenmodes into the r-dominated internal mode can occur near an avoided crossing *if* a collision has enough kinetic energy to access these avoided crossing regions. From Fig. 4(d), which pertains to the collinear geometry case, we note that avoided crossings do not occur at all, at least within the energy range studied. This combines with the bending mode's geometric instability of the linear structures to further emphasize the importance of near-C_{2v} geometries relative to near-collinear geometries.

B. Relation to reaction thresholds

For all of the species considered here, as shown in Figs. 4(a)–4(c), the avoided crossings occur at geometries where the potential energy is considerably in excess of either the thermodynamic threshold or the barrier on the C_{2v} potential surface. In Table II, the interfragment distances (R) at which the avoided crossings occur (i.e., where the splitting between interacting MWH eigenvalues are smallest) are listed as are the potential energies at these geometries. The experimental thresholds for formation of MH^+ and MD^+, where known, are also listed.

It should be noted that the interactions among modes that gives rise to the avoided crossings do not exist *only* at the R values listed in Table II. Such interactions are present over a significant range of interfragment distances, and certainly develop significant strength somewhat before reaching the R values listed. For this reason, we specify lower bounds to the critical interaction distances when we quote geometries where the MWH eigenvalues come closest. Moreover, because the potential energy surfaces are quite "steep" and repulsive in these regions, the *energies* derived at our quoted R values *represent upper bounds* to the minimum energies needed to effect reaction.

Having made these qualifying remarks, the model dynamics provided by the MWH eigenmode analysis *explains*

the reaction thresholds in terms of the avoided crossings. When the kinetic energy of collision $T_{\text{collision}}$ is large enough to access geometries where the MWH eigenvalues undergo avoided crossings, energy transfer to the internal mode (r) induces reaction. As interfragment collisional kinetic energy is lost, energy is deposited into the internal mode, thereby causing the H–H (D–D or H–D) bond to lengthen and to eventually rupture. The geometries at which these avoided crossings occur are typified by strong

repulsive forces along *both* r_{MH} and $r_{\text{MH}'}$ (or r_{MD}) axes. Therefore collisions that access these regions must have high kinetic energies along both of these axes. For this reason, it is the *total* kinetic energy, not T_{MA} or T_{MB}, that is the key collision energy parameter.

The data summarized in Table II clearly show, e.g., that thresholds for B^+, Al^+, and Ga^+ reacting with D_2 should occur ~1.3, 2.5, and 3.3 eV above their respective endothermicities. Although our predicted thresholds dis-
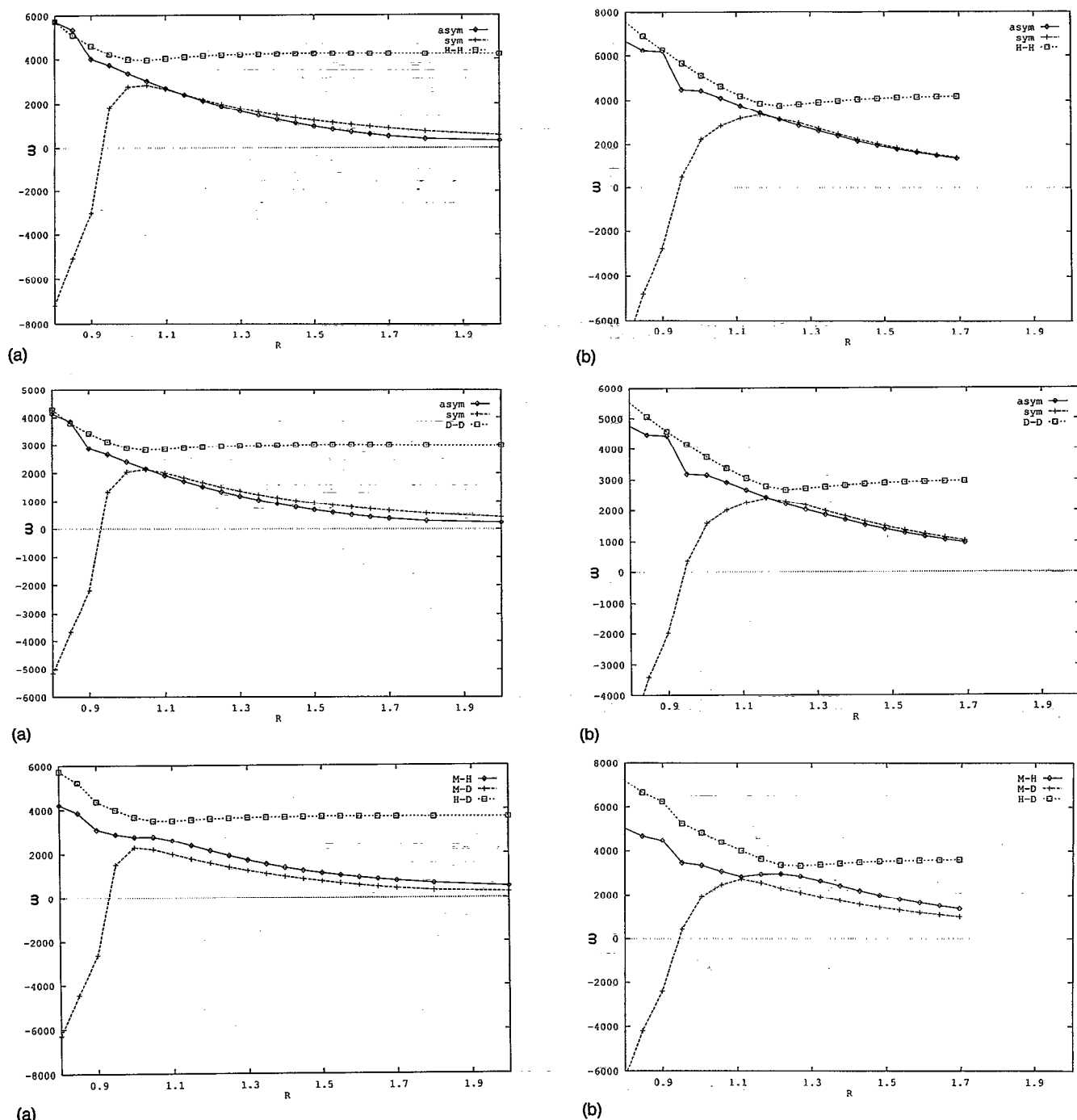

FIG. 4. Avoided crossings of eigenvalues of the mass-weighted Hessian matrix for (a) $B^+ + H_2$, D_2, and HD; (b) $Al^+ + H_2$, D_2, and HD; and (c) $Ga^+ + H_2$, D_2, and HD. In (a)–(c), the horizontal axis is R (in Ångstroms) and the vertical axis is ω (cm^{-1}). For large R, the highest frequency mode is the HH, DD, or HD stretching vibration, and the lower two are the relative-motion modes. (d) The plot of eigenvalues of the mass-weighted Hessian matrix for $B^+ + H_2$, D_2, and HD in collinear geometries with the H–H stretch, interfragment, and bending vibrations labeled. The horizontal axis is R (Ångstroms) and the vertical axis is ω (cm^{-1}).
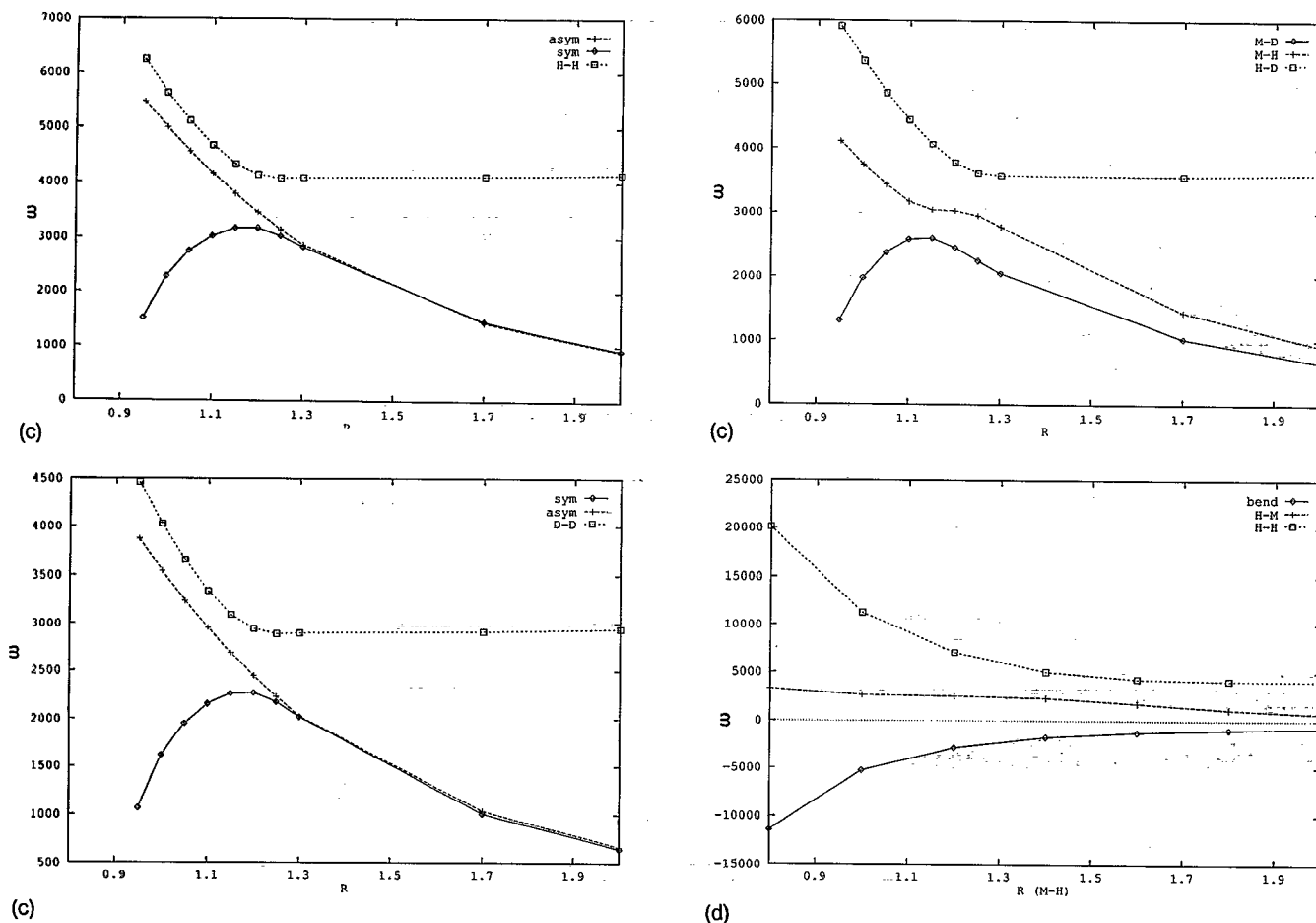
FIG. 4. (*Continued.*)

play trends much like the experimental findings (see Table II), the energies where the avoided crossings are strongest tend to systematically exceed the experimental thresholds by ~1 eV (see comments above about upper bounds). This is likely a result of the steeply repulsive nature of the potentials (e.g., the energies drop by more than 1 eV over a 0.05 Å range of R in these regions for all three species) at such geometries and the fact that significant mode coupling develops at longer R values than where the avoided crossing is strongest. In addition, the thermal motions of H$_2$, D$_2$, or HD are nonzero and tend to make the apparent experimental thresholds lower than the true thresholds.

C. Isotope effects for HD

In the HD cases, the two relative-motion modes have different natural frequencies; the mode dominated by r_{MH} motion has higher frequency than that dominated by r_{MD}. As a result, the former mode undergoes an avoided crossing with the internal (r-dominated) mode at larger R, and hence at lower energy. Energy that is thus transferred from the r_{MH} motion to the internal mode decreases the relative velocity along r_{MH}, but not (as much) along r_{MD}. The differential velocity that thus develops between r_{MD} and r_{MH} causes the M-to-D distance to shorten more rapidly than the M-to-H distance, while the H-to-D distance is

growing (since energy is being put into this mode to break the H–D bond). As these movements propagate in time, MD$^+$ is formed and H is eliminated.

The important point is that the *lower-energy avoided crossing* involves coupling energy out of the r_{MH} mode and *production of* MD$^+$+H. Likewise, the *higher-energy avoided crossing*, which involves the r_{MD}-dominated mode coupling to the H–D motion, *produces* MH$^+$+D. The difference in thresholds for MD$^+$ and MH$^+$ formation is explained by differences in the energies at which the r_{MH} and r_{MD} avoided crossings occur.

D. Coupling strengths

The avoided crossing graphs also provide information about the strength of coupling between the relative-motion and internal modes. When the eigenvalues $\omega^2_\pm$ that "avoid" one another are viewed as solutions of a 2×2 matrix eigenvalue problem, the difference $(\omega^2_+ - \omega^2_-)$ between them can be related to the off-diagonal element of the matrix (which we denote Ω and which has units of s^{-2})

$$\Omega = \frac{(\omega^2_+ - \omega^2_-)}{2}.$$

In Table II, we also report these coupling strengths $\sqrt{\Omega}$ (in cm^{-1} units) for all of the cases considered here. Thus far,

we have not made a direct connection between these coupling strengths and experimental findings. Clearly, they relate to the magnitude of energy flow between the relative-motion and internal modes near the avoided crossing, but their magnitudes do not seem to correlate with ion yield or branching ratio [e.g., Ω is larger for coupling to the r_{MH} mode than to the r_{MD} mode, although the yield (of MD$^+$) from the former is smaller than for the latter]. Of course, the observed ion yields are not direct measures of the *initial* rate of formation of MD$^+$ or MH$^+$ because nascent ions may undergo decomposition before being detected, and the fraction that decomposes depends on the collision energy E.

E. Long interaction times are required

Not only must a "trajectory" access the avoided crossing geometry, it must spend enough time there to permit the couplings to effect energy transfer. The time (τ) spent in this region can be estimated in terms of the initial collision energy E_{coll}, the range of R values over which the coupling takes place ΔR, the electronic potential energy near the avoided crossing V_{cross} as well as the reduced mass μ of the M$^+$+A–B pair

$$\mu = \frac{m_{AB} + m_M}{m_{AB} + m_M}, \quad \tau = \frac{\Delta R}{\sqrt{2(E_{\text{coll}} - V_{\text{cross}})/\mu}}.$$

The time needed to effect energy transfer is related to the strength of coupling between the two modes undergoing the avoided crossing. As shown earlier, this coupling (Ω in s^{-2}) can be extracted from the avoided crossing graphs as one-half the "splitting" between the two eigenvalues at their closest approach $\Omega = (\omega_+^2 - \omega_-^2)/2$. So, if

$$\tau\sqrt{\Omega} = \frac{1}{\sqrt{2}} \frac{\Delta R \sqrt{(\omega_{\text{high}}^2 - \omega_{\text{low}}^2)}}{\sqrt{2(E_{\text{coll}} - V_{\text{cross}})/\mu}} \gg 1,$$

energy transfer can be facile. This implies that collisions with incident kinetic energies slightly in excess of V_{cross} will be most effective in transferring energy into the r-dominated degrees of freedom, and that collisions with

much higher kinetic energy should be less effective. For the cases considered here, as shown in Table II, $1/\sqrt{2}\sqrt{(\omega_{\text{high}}^2 - \omega_{\text{low}}^2)}$ ranges from ~ 952 to 1953 cm^{-1} (i.e., corresponding to frequencies of 3–6×10^{13} s^{-1}) and ΔR ranges from 0.05 to ~ 0.2 Å. Therefore, one expects collisions passing through the avoided crossing region at $\sim 10^4$–10^5 cm s^{-1} or slower to be quite effective. This means that collisions with kinetic energy along the collision mode to which r is coupled much in excess of the potential at the avoided crossing will be ineffective.

F. The fate of collisions that result in energy transfer

Those collisions that access geometries where energy transfer from a relative-motion coordinate to an internal mode can occur have a chance to evolve to produce MH$^+$ (or MD$^+$) product ions. In doing so, the H–H (D–D or H–D) bond breaks, a new M–H (or M–D) bond is formed, and an H (or D) is eliminated.

In the picture provided by the MWH eigenmode model, once enough energy and momentum are transferred to the r coordinate, flux can evolve toward larger r values. Such flux will move toward the barrier regions of the potential energy surfaces shown in Fig. 1, although the total energy exceeds the barrier energy (of 3.2, 4.5, and 4.6 eV for B$^+$, Al$^+$, and Ga$^+$, respectively) by more than 1 eV in all cases.

However, as flux so evolves, our analysis of the three potential surfaces in Fig. 1 shows that a region on the $^1A_1$ potential surface is reached within which either (i) the asymmetric stretch motion of b_2 symmetry becomes unstable (i.e., develops a negative MWH eigenvalue) due to second-order Jahn–Teller coupling with the nearby $^1B_2$ excited state or (ii) the $^1B_2$ excited state intersects and passes below the $^1A_1$ surface. In either case, flux can move, with no restoring forces, away from C_{2v} symmetry. It is *this step* that *permits the asymmetric rupture of the* MH$_2^+$ *species* to produce the observed MH$^+$ (or MD$^+$)+H (or D). In Tables III are shown the geometries at which the $^1B_2$ state has its own minimum because it is near such geometries

TABLE II. Geometry, energy, and coupling strength in the region of avoided crossing of mass-weighted Hessian eigenvalues and experimental reaction thresholds.

Species	R at crossing (Å)	ΔE_{thermo} (eV)[b]	E at crossing (kcal/mol; eV)	Coupling strength $\sqrt{\Omega}$ (cm^{-1})	Experimental thresholds[a] (eV) to form (MA$^+$)
B$^+$+HH	>1.05	2.6	<89; 3.9	1953	3.3±0.1
B$^+$+DD	>1.05		<89; 3.9	1302	3.3±0.1
B$^+$+HD	>1.00 (r_{MD})		<107; 4.6	1121	4.0±0.2 (BH$^+$)
	>1.05 (r_{MH})		<89; 3.9	1502	3.0±0.2 (BD$^+$)
Al$^+$+HH	>1.22	3.9	<148; 6.4	1352	6.6±0.2
Al$^+$+DD	>1.22		<148; 6.4	952	6.6±0.1
Al$^+$+HD	>1.16 (r_{MD})		<177; 7.7	1070	6.7±0.1 (AlH$^+$)
	>1.22 (r_{MH})		<148; 6.4	1121	4.7±0.1 (AlD$^+$)
Ga$^+$+HH	>1.21	4.1	<170; 7.4	1881	Not available
Ga$^+$+DD	>1.21		<170; 7.4	1323	8.5±0.5 (GaD$^+$)
Ga$^+$+HD	>1.15 (r_{MD})		<206; 9.0	1120	Not available
	>1.25 (r_{MH})		<145; 6.3	1483	

[a]Reference 1 as well as P. B. Armentrout (private communication).
[b]Not zero-point corrected, so independent of isotopic masses.

TABLE III. Total and relative energies, geometries, and vibrational frequencies for species relating to (A) the $B^+ + H_2 \rightarrow BH^+ + H$, HBH^+ reactions; (B) the $Al^+ + H_2 \rightarrow AlH^+ + H$, $HAlH^+$ reactions; and (C) the $Ga^+ + H_2 \rightarrow GaH^+ + H$, $HGaH^+$ reactions.

(A)	Species	Electronic energies (hartrees)	Optimized internuclear distances (Å)	Vibrational frequencies[b]/ zero point energies (cm^{-1})	Relative energies (kcal/mol)[a]
	$B^+(^1S) + H_2$	$-25.446\,250$	$r = 0.755$	4224/2112	0.0
		$-25.468\,830$			0.0
	$BH^+(^2\Sigma) + H$	$-25.351\,373$	$r_{BH} = 1.199$	2582/1291	60
		$-25.372\,139$			61
	$HBH^+(^1\Sigma_g^+)$	$-25.520\,364$	$r = 2.374$	2594 (a_1),	-47
		$-25.564\,074$		2880 (b_2),	-60
				932 (bend)/3669	
	$B^+ \cdots H_2$ barrier	$-25.322\,627$	$r = 1.396$	4512i (a_1),	78
		$-25.352\,085$	$R = 1.226$	1279 (a_1),	73
				3424i (b_2)	
	$BH_2^+(^1B_2)$	$-25.328\,460$	$r = 1.674$	1026 (a_1),	74
	minimum	$-25.399\,644$	$R = 0.996$	2173 (b_2),	43
				2083 (a_1)/2641	

(B)	Species	Electronic energies (hartrees)	Optimized internuclear distances (Å)	Vibrational frequencies[b]/ zero point energies (cm^{-1})	Relative energies (kcal/mol)[a]
	$Al^+(^1S) + H_2$	$-242.856\,705$	$r = 0.755$	4224/2112	0.0
		$-242.879\,646$			0.0
	$AlH^+(^2\Sigma) + H$	$-242.717\,076$	$r_{AlH} = 1.658$	1424/712	88
		$-242.735\,419$			91
	$HAlH^+(^1\Sigma_g^+)$	$-242.804\,625$	$r = 3.103$	1940 (a_1),	33
		$-242.860\,474$		2055 (b_2),	12
				513 (bend)/2511	
	$Al^+ \cdots H_2$ barrier	$-242.692\,731$	$r = 1.852$	2362i (a_1)	103
		$-242.713\,641$	$R = 1.587$	1942i (b_2)	104
				996 (a_1)	
	$AlH_2^+(^1B_2)$	$-242.685\,868$	$r = 1.729$	855 (a_1),	107
	minimum	$-242.740\,915$	$R = 1.429$	1307 (b_2),	87
				1637 (a_1)/1900	

(C)	Species	Electronic energies[c] (hartrees)	Optimized internuclear distances (Å)	Vibrational frequencies[b]/ zero point energies (cm^{-1})	Relative energies (kcal/mol)[a]
	$Ga^+(^1S) + H_2$	$-258.119\,452$	$r = 0.757$	4224/2112	0.0
		$-1\,924.206\,695$			0.0
	$GaH^+(^2\Sigma) + H$	$-257.967\,714$	$r_{GaH} = 1.747$	902/451	83
		$-1\,924.056\,193$	$r_{GaH} = 1.65$		94
	$HGaH^+(^1\Sigma_g^+)$	$-258.069\,058$	$r = 3.096$	2003 (a_1),	32
		$-1\,924.174\,511$		2139 (b_2),	20
				628 (bend)/2699	
	$Ga^+ \cdots H_2$ barrier		$r = 2.0$	Not available[d]	105
			$R = 1.75$		
	$GaH_2^+(^1B_2)$	$-257.909\,068$	$r = 1.886$		132
	minimum	$-1\,923.991\,427$	$R = 1.390$		135

[a]In all cases, the energies are given relative to the $B^+ + H_2$ reactants in (A), the $Al^+ + H_2$ reactants in (B) and the $Ga^+ + H_2$ reactants in (C). These are electronic energies, and thus do not include zero-point corrections. In each case, and for the column giving total energies in hartrees, the first number is based on our CAS-MCSCF calculations, and the second is based on our QCISD(T) data.

[b]These local harmonic frequencies were obtained from the analytical second derivatives of the MCSCF energy at the MCSCF geometries.

[c]The MCSCF calculations used a pseudopotential, but the QCISD(T) data involve all electrons.

[d]The finite difference routines used in GAMESS were not able to produce a reliable Hessian matrix in this case.

that the second-order Jahn–Teller couplings or surface intersections are most likely. Also shown in Tables III are the eigenvalues of the MWH at the barrier geometry; in all cases, one notes an imaginary frequency for the b_2 mode, which reflects the geometrical instability of these regions to asymmetric distortion.

Because the regions of avoided crossings of MWH eigenvalues occur high above the barrier regions, the MH$^+$ (or MD$^+$) product ions are likely to be formed with a large amount of internal (vibration/rotation) and translational energy. Because the M–H$^+$ bond strengths are rather weak (48, 18, and 15 kcal/mol for BH$^+$, AlH$^+$, and GaH$^+$, respectively), such internal energy can cause the nascent MH$^+$ species to fragment before reaching the experiment's detector. Hence, fragmentation of the product ions can contribute to the unusually small cross sections[1] found for these reactions, although another cause is likely to be the severe "steric" requirments imposed by reaching the region of strong mode coupling and the inefficient relative-motion to internal-motion energy flow.

VI. SUMMARY

Energies at which the local natural frequencies corresponding to interfragment and to internal motions (obtained as eigenvalues of the full $3N$-6 or $3N$-5 dimensional MWH matrix) undergo avoided crossings are related to kinetic energy thresholds in the ion–molecule reactions M$^+$+H$_2 \rightarrow$MH$^+$+H, for M$^+$=B$^+$, Al$^+$, and Ga$^+$ and deuterium substituted analogs. At collision energies substantially in excess of the avoided crossings, there may not be adequate "contact time" to permit energy transfer to occur; at collision energies much below the avoided crossing, the resonance condition is not met, and energy cannot flow. This model predicts that it is the *total* kinetic energy of collision $T_{\text{collision}}$, not its components T_{MA} and T_{MB} along the two M-to-H (or D) axes, that is important in determining the reaction threshold because it is this energy that governs whether a collision can access the regions of the potential surface where avoided crossings occur.

Although systematic differences exist between the apparent experimental thresholds and our (upper bound) predictions, the trends seem to be in agreement. Moreover, the fact that thresholds exceed thermodynamic requirements is reproduced by our model, as is the propensity to produce MD$^+$ at lower collision energy than MH$^+$.

The primary assumption in making correlations between reaction thresholds and avoided crossings of the MWH eigenvalues is that energy transfer in such mode-coupling collisions is the rate determining step in forming MH$^+$ products. Such a model was introduced because the experimentally observed reaction thresholds exceed by 0.4 to $\sim$5 eV the thermodynamic energy requirements or computed barrier heights of these reactions and because the measured cross sections are very small. This is, of course, not true for all ion–molecule reactions, but is for the "impulsive" reactions considered here.

The fact that the avoided crossings occur high above the thermodynamic thresholds leads to large internal energies in the MH$^+$ (or MD$^+$) product ions and to likely

subsequent dissociation. This is one of the likely causes for the measured cross sections for MH$^+$ (or MD$^+$) formation being small (smallest for Ga$^+$ and largest for B$^+$).

Preference to form MD$^+$ at lower collision energies than MH$^+$ when HD reacts with M$^+$ is consistent with the avoided-crossing frequency-resonance picture introduced here. The higher frequency M–H mode (which leads to MD$^+$ products) couples to the high frequency internal motion (H–D) mode at larger R values (and hence lower energy) than the lower frequency M–D mode.

Although the MWH matrix is used as a tool in this analysis, the model put forth here is *not* equivalent to a reaction path Hamiltonian[2] dynamics model, which also employs the MWH. The latter as well as the gradient extremal method[11] use the gradient itself to define the "special" direction of the reaction path connecting a transition state (i.e., a first-order saddle point on the energy surface) to the reagent geometry. The critical geometries of our approach (those where avoided crossings of MWH eigenvalues occur) can have energies much in excess of the nearest first-order saddle points, and they need not even be close to the usual minimum-energy[2] or gradient extremal[11] path. At points we consider, the gradient often has large components along both inter- and *intra*fragment degrees of freedom, unlike the case for reaction paths. The geometries along the path we use relate to trajectories that would be realized in high-energy ion–molecule collisions in which the reagents have little internal energy.

[1] P. B. Armentrout, Int. Rev. Phys. Chem. **9**, 115 (1990); J. L. Elkind and P. B. Armentrout (unpublished results); S. A. Ruatta, L. Hanley, and S. L. Anderson, J. Chem. Phys. **91**, 226 (1989).
[2] W. H. Miller, N. C. Handy, and J. E. Adams, J. Chem. Phys. **72**, 99 (1980).
[3] T. Dunning, J. Chem. Phys. **90**, 1007 (1989).
[4] A. D. McLean and G. S. Chandler, J. Chem. Phys. **72**, 5639 (1980).
[5] W. J. Stevens, H. Basch, and M. Krauss, J. Chem. Phys. **81**, 6026 (1984).
[6] R. Krishnan, J. S. Binkley, R. Seeger, and J. A. Pople, J. Chem. Phys. **72**, 650 (1980).
[7] (a) The Utah MESS-KIT is a suite of highly modular codes that were programmed in house to give a variety of electronic structure functionalities by J. A. Nichols, M. R. Hoffmann, R. A. Kendall, H. L. Taylor, D. W. O'Neal, E. Earl, R. Hernandez, M. Gutowski, J. Boatz, K. Bak, J. Anchell, X. Wang, M. Feyereisen, and J. Simons; (b) J. Nichols, H. Taylor, P. Schmidt, and J. Simons, J. Chem. Phys. **92**, 340 (1990); J. Simons, P. Jørgensen, H. Taylor, and J. Ozment, J. Phys. Chem. **87**, 2745 (1983); D. O'Neal, H. Taylor, and J. Simons, *ibid.* **88**, 1510 (1984); A. Banerjee, N. Adams, J. Simons, and R. Shepard, *ibid.* **89**, 52 (1985); H. Taylor and J. Simons, *ibid.* **89**, 684 (1985); C. J. Cerjan and W. H. Miller, J. Chem. Phys. **75**, 2800 (1981); J. Baker, J. Comp. Chem. **9**, 465 (1988); **7**, 385 (1986).
[8] (a) M. Dupuis, D. Spangler, and J. J. Wendolowski, National Resource for Computations in Chemistry Software Catalog, University of California, Berkeley, 1980, program OG01; (b) M. W. Schmidt, K. K. Baldridge, J. A. Boatz, J. H. Jensen, S. Koseki, M. S. Gordon, K. A. Nguyen, T. L. Windus, S. T. Elbert, QCPE Bull. **10**, 52 (1990).

[9] M. J. Frisch, M. Head-Gordon, G. W. Trucks, J. B. Foresman, H. B. Schlegel, K. Raghavachari, M. A. Robb, J. S. Binkley, C. Gonzales, D. J. DeFrees, D. J. Fox, R. A. Whiteside, R. Seeger, C. F. Melius, J. Baker, R. L. Martin, L. R. Kahn, J. J. P. Stewart, S. Topiol, and J. A. Pople, Gaussian '90, Gaussian Inc. Pittsburgh, 1990.

[10] J. Simons, *Energetic Principles of Chemical Reactions* (Jones and Bartlett, Portola Valley, CA, 1983).

[11] D. K. Hoffman, R. S. Nord, and K. Ruedenberg, Theor. Chim. Acta **69**, 265 (1986).

[12] See, e.g., *Classical Dynamics of Particles and Systems*, edited by J. B. Marion (Academic, Orlando, Fla., 1970), pp. 409–415.

[13] See, e.g., C. Jaffe and P. Brumer, J. Chem. Phys. **73**, 5646 (1980); E. L. Sibert III, W. P. Reinhardt, and J. T. Hynes, *ibid.* **77**, 3583 (1982) for applications to near-resonant energy transfer in small molecules.